Uniaxial-deformation behavior of ice I_h as described by the TIP4P/Ice and mW water models

Pedro Antonio Santos-Flórez, Carlos J. Ruestes, and Maurice de Koning

Citation: J. Chem. Phys. **149**, 164711 (2018); doi: 10.1063/1.5048517
View online: https://doi.org/10.1063/1.5048517
View Table of Contents: http://aip.scitation.org/toc/jcp/149/16
Published by the American Institute of Physics

Uniaxial-deformation behavior of ice I_h as described by the TIP4P/Ice and mW water models

Pedro Antonio Santos-Flórez,[1,a)] Carlos J. Ruestes,[2,b)] and Maurice de Koning[1,3,c)]
[1]*Instituto de Física Gleb Wataghin, Universidade Estadual de Campinas, UNICAMP, 13083-859 Campinas, São Paulo, Brazil*
[2]*CONICET and Facultad de Ciencias Exactas y Naturales, Universidad Nacional de Cuyo, Mendoza, Argentina*
[3]*Center for Computational Engineering and Sciences, Universidade Estadual de Campinas, UNICAMP, 13083-861 Campinas, São Paulo, Brazil*

(Received 15 July 2018; accepted 5 October 2018; published online 30 October 2018)

Using molecular dynamics simulations, we assess the uniaxial deformation response of ice I_h as described by two popular water models, namely, the all-atom TIP4P/Ice potential and the coarse-grained mW model. In particular, we investigate the response to both tensile and compressive uniaxial deformations along the [0001] and [$0\bar{1}10$] crystallographic directions for a series of different temperatures. We classify the respective failure mechanisms and assess their sensitivity to strain rate and cell size. While the TIP4P/Ice model fails by either brittle cleavage under tension at low temperatures or large-scale amorphization/melting, the mW potential behaves in a much more ductile manner, displaying numerous cases in which stress relief involves the nucleation and subsequent activity of lattice dislocations. Indeed, the fact that mW behaves in such a malleable manner even at strain rates that are substantially higher than those applied in typical experiments indicates that the mW description of ice I_h is excessively ductile. One possible contribution to this enhanced malleability is the absence of explicit protons in the mW model, disregarding the fundamental asymmetry of the hydrogen bond that plays an important role in the nucleation and motion of lattice dislocations in ice I_h. *Published by AIP Publishing.* https://doi.org/10.1063/1.5048517

I. INTRODUCTION

The mechanical properties of water ice play a central role in a wide variety of phenomena in such different fields as glaciology, climatology, materials science, and engineering and take place on vastly different time and length scales.[1–3] For example, the flow of glaciers and ice sheets, which takes place on time and length scales of years and kilometers, respectively, is directly involved in the slow dynamics of Earth's global climate system. On the other hand, the high-velocity impact of pieces of ice with ice-breaker ships, bridge pillars, and aircraft parts involve processes that occur on time and length scales of seconds and meters and affect the integrity of such man-made engineering structures.

While there are at least 19 crystalline and 3 amorphous forms in its phase diagram,[1] under the thermodynamic conditions on Earth, the proton-disordered hexagonal ice I_h is the only relevant crystalline form of water. Yet, this single phase displays an astonishing richness in its mechanical properties. Not only can ice I_h behave as a brittle solid, as one usually observes in daily experience, it can also deform in a ductile manner by flowing along basal planes, depending on factors such as deformation rate and temperature.[4] In fact, Glen and Perutz[5] verified experimentally that, under the application of low stresses (~0.1-0.5 MPa), strains of up to 600% could be reached without apparent macroscopic failure.

The mechanical characteristics of ice have become the focus of substantial research efforts over the past decades.[5–21] Most of these have been experimental in character, focusing mainly on the phenomenological aspects of the deformation behaviors. Much less is known, however, about the molecular-scale processes that underlie these behaviors. For instance, except for insight into the molecular structure of partial dislocations on the basal plane from first-principles calculations on ice I_h,[22] not even the basic molecular-scale mechanism for their motion in ice is understood. While X-ray topography permits the visualization of extended defects and their motion in ice on the scale of millimeters,[23–26] an experimental technique that offers nano-scale visualization—such as that provided by *in situ* transmission electron microscopy (TEM) for the case of metals,[27]—remains unavailable.

In this context, atomistic-level simulation has proven an extremely useful alternative route of investigation. It constitutes a method for *in situ* computational "microscopy,"[28] which provides detailed insight into the unit mechanisms that operate on atomic length and time scales. For this reason, such simulations are commonplace in physics, chemistry, and materials science and they have been applied innumerous times to investigate the fundamental mechanisms that control the mechanical properties of crystalline and amorphous solids.[29,30] Water ice, however, has been a notable

[a)]Electronic mail: pasantos@ifi.unicamp.br
[b)]Electronic mail: cruestes@fcen.uncu.edu.ar
[c)]Electronic mail: dekoning@ifi.unicamp.br

exception. Although countless simulations have focused on various aspects of the condensed phases of water, including their structural, dielectric, thermodynamic, and kinetic properties,[31–56] the mechanical behavior of ice, with the exception of three recent studies concerning the modeling of atomic force microscopy indentation,[57] methane hydrates,[58] and shock Hugoniots,[59] has remained largely out of scope. Indeed, the development process of molecular models by itself, with the objective of proposing interatomic potentials that improve the description of the behaviors of water across different phases,[52] has for the most part neglected the mechanical properties of crystalline and amorphous phases of water. This implies that the mechanical response of the many water models developed over the past decades are essentially unknown.

In this paper, we investigate the mechanical response of ice I_h for two of the most popular water models that have been used to describe solid phases of water, namely, the all-atom TIP4P/Ice model[32,33,36,51,53–55] and the coarse-grained mW potential.[38,40,43–45,56] The former is a reparametrization of the original TIP4P model[60] with the objective of improving the description of ice phases. The mW model, on the other hand, is an adaptation of Stillinger and Weber's silicon potential[61] with the intent of modeling the interactions between water molecules without explicitly considering the protons and the long-range electrostatic interactions. In particular, we focus on the behavior of the systems subjected to uniaxial deformation, both tensile and compressive in nature, investigating the respective mechanisms of failure. In particular, the specific dependence of the failure mode on parameters such as deformation rate and temperature is indicative of intrinsic brittle or ductile behavior and thus of interest in the context of characterizing the mechanical response of both water models for ice I_h.

II. COMPUTATIONAL APPROACH

A. Generation of computational cells

The majority of the simulations were carried out using a periodic cell containing 12 800 water molecules, with spatial dimensions $16 \times 10 \times 10$ in units of the a, b, and c directions of the conventional orthogonal unit cell containing 8 molecules.[62] To assess possible cell-size effects, a smaller number of simulations were executed using a $36 \times 18 \times 18$ cell containing 93 312 molecules. Both cells represent fully proton-disordered realizations of a defect-free I_h structure with zero total dipole moment. They were generated as follows. First, we generate the positions of the oxygen atoms, placing them on the sites of the Wurtzite lattice. Next, we attach two protons to each of them to form water molecules. But given the proton-disordered nature of ice I_h, this must be performed randomly but subject to the constraint imposed by the second Bernal-Fowler ice rule which requires that there be precisely one proton between each nearest-neighbor pair of oxygen atoms.[1] For a periodic, defect-free ice I_h cell, this can be achieved using the approach of Rahman and Stillinger.[63] It amounts to mapping the assignment of molecular orientations onto the problem of generating a 3-dimensional *directed* graph in which each node is connected to four neighbors arranged according to the Wurtzite lattice, with precisely two ingoing and two outgoing links. In this network picture, the nodes represent the oxygen atoms, and the two outgoing links of each node correspond to the two protons that are covalently bonded to it in the water molecule. To generate such a directed graph, we start with its *undirected* counterpart and search for a cyclic decomposition using a series of random walks. This proceeds as follows. Starting from the undirected graph, we randomly select a vertex and initiate a random walk in which each hop consists of a move from a given site to one of its 4 nearest neighbors in the Wurtzite lattice. Keeping track of the path traveled by the walker, it is terminated whenever it visits a vertex for a second time. The part of the path that lies between the first and second visits of this vertex comprises a *cycle* in the lattice. All the links in it are then directed in the direction traveled by the walker, whereas the remaining (i.e., non-cyclic path) part of the path is erased. Excluding the directed links in the cycle from further visits, a new random walker is initiated to find a second cycle and this procedure is repeated until no undirected links remain and the entire graph has been randomly decomposed into cycles. After finding such a random cyclic decomposition, the generated directed network is composed of a set of closed paths in which, by construction, each link of the network has been traversed exactly once, with each node having precisely two incoming and two outgoing links. If the cyclic decomposition has a non-zero total dipole moment due to closed paths that cross the periodic boundary conditions,[63] it may be possible to eliminate it by inverting the direction of a number of them. If this is not possible, we repeat the procedure starting from the original undirected graph until a cell with zero total dipole moment is obtained. Only for the 93 312-molecule cell we did need two runs to find a zero-dipole-moment configuration.

B. Simulation protocols

All simulations have been carried out using molecular dynamics techniques as implemented in the Large-scale Atomic/Molecular Massively Parallel Simulator (`LAMMPS`) package.[64] In all cases, prior to deformation, the ice I_h cells were equilibrated at zero pressure and the desired temperature. We consider 3 temperatures for each water model, namely, 50 K and 200 K for both of them, and a third value ~5 K below their corresponding melting temperatures, giving 264 and 269 K, respectively, for the TIP4P/Ice and mW models. Equilibration was achieved by running simulations within an anisotropic zero-pressure isobaric-isothermal *NPT* ensemble in which all three sides of the orthogonal cell are allowed to vary independently. The corresponding equations of motion are based on a Parrinello-Rahman-type barostat[65–67] and a Langevin thermostat.[68]

For the TIP4P/Ice all-atom model, bond lengths and angles are held fixed using the `SHAKE` algorithm,[69] and the long-range electrostatics is handled employing the particle-particle particle-mesh (PPPM) scheme.[70] The equations of motion are integrated using a time step of $\Delta t = 0.5$ fs, and the damping time scales for the thermostat and barostat were chosen as $\tau_T = 0.2$ ps and $\tau_p = 2$ ps, respectively. Compared to the TIP4P/Ice model, the only difference for the mW model is the integration time step, chosen at

Δt = 1 fs. Of course, the SHAKE and PPPM methods are unnecessary to begin with for the charge-neutral atomic mW model.

After the initial equilibration, the computational cells are isothermally deformed under controlled conditions of strain rate, adopting a protocol similar to that employed by Wu and Prakash in their investigation of the mechanical stability of methane hydrates.[18] Specifically, we apply uniaxial deformations by uniformly rescaling the position components along the axis of deformation at each step. This rescaling is carried out in the spirit of the $NL_dP_1P_2T$ ensemble, in which L_d is the length of the cell along the deformation direction and P_1 and P_2 are the transverse pressure components. In all the deformation simulations, L_d varies with time according to $L_d(t) = L_{d0}(1 + \dot{\varepsilon}\, t)$, with $\dot{\varepsilon}$ being the strain rate and L_{d0} being the initial length of the deformation axis, while maintaining $P_1 = P_2 = 0$ throughout the entire deformation simulation. This allows expansion or contraction of the transverse directions of the cell associated with the Poisson effect during compressive or tensile uniaxial deformations. Even though the employed strain rates are substantially higher than those used in typical laboratory experiments, the obtained results provide valuable insight into the intrinsic mechanical behavior of the two water models.

In all considered cases, different realizations of the same deformation process were not found to display significant quantitative nor qualitative differences. Accordingly, all stress-strain curves reported below correspond to the results obtained from single deformation simulations, without ensemble averaging.

Furthermore, for all considered deformation rates, the maximum attained strain values in the simulations for the mW model have been chosen to be approximately twice as large as those for the TIP4P/Ice model. As will become clear in the following, this choice is motivated by the distinct mechanical response for both models. Whereas the failure mode for the TIP4P/Ice model is characterized by a single deformation event, the response of the mW model often displays a succession of further occurrences after the first yield drop, giving rise to strongly non-monotonic behavior of the stress-strain curves up to substantially larger strain values. To explore this behavior, the deformation simulations involving the mW model cover time intervals that are roughly twice as long as those for the TIP4P/Ice model for a given strain rate.

III. RESULTS AND DISCUSSION

A. Tensile deformation

We first consider the results obtained for the simulations in which the computational cells were subjected to uniaxial tensile deformation. The top row of Fig. 1 presents the stress-strain response for tensile deformations along the [0001] axis on the 12 800-molecule cell, comparing the two water models at temperatures varying between 50 K and the vicinity of the melting point, at a strain rate $\dot{\varepsilon} = 5 \times 10^7$ s^{-1}. For small strains, all systems display the expected linear elastic behavior. In particular, the TIP4P/Ice model features a Young's modulus starting at 11 GPa at 50 K and decreasing to 10 GPa as temperature increases to 264 K. For the mW model, the values decrease from 11.5 GPa at 50 K to 9 GPa at 269 K. Both models are consistent with experimental data,[71] which give values decreasing from ~12.8 GPa at 200 K to ~11.8 GPa at 257 K. For strains of the order of 0.10, the elastic response becomes nonlinear, closely followed by a yield point. As expected, both the critical strain and the stress at the yield point decrease with increasing temperature.

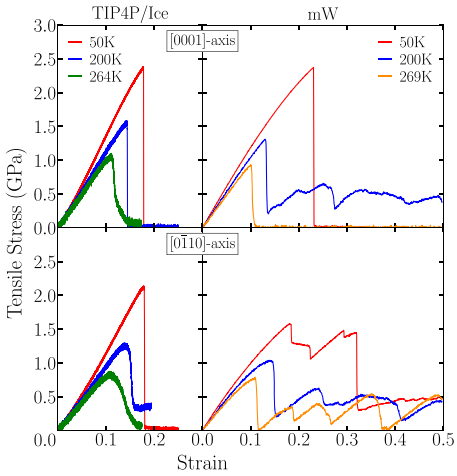

FIG. 1. Stress-strain curves for the tensile deformation at strain rate of 5×10^7 s^{-1} along the c-axis and the [0$\bar{1}$10] axis for TIP4P/Ice and mW models for the 12 800-molecule cell at different temperatures.

To characterize the mode of failure, we visualize structures along the deformation process using the identify-diamond-structure[72] algorithm incorporated into the Open Visualization Tool (OVITO) package.[73] It distinguishes between cubic and hexagonal-diamond structures by analyzing the arrangement of the second-nearest neighbors of a given oxygen atom. Full details can be found in Ref. 72.

Typical results for the TIP4P/Ice model are shown in Fig. 2. At T = 50 K and T = 200 K, the failure is brittle in nature, characterized by complete cleavage along the basal plane. At 264 K, which is 5 K below the melting temperature T_m, failure no longer involves cleavage, and stress relief is achieved by partial melting.

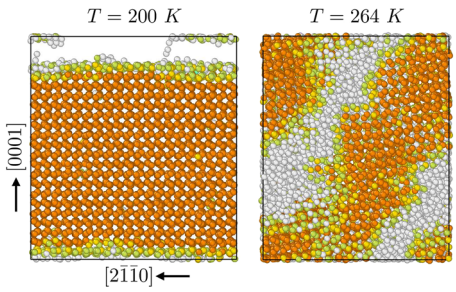

FIG. 2. Typical failure modes in tensile tests along the c axis for the TIP4P/Ice model and the 12 800-molecule cell at a strain rate of 5×10^7 s^{-1}. Colors of particles indicate different crystal symmetries as identified by OVITO: Wurtzite (orange), Wurtzite first neighbor (yellow), Wurtzite second neighbor (green). White particles belong to disordered regions. Brittle failure through cleavage at 0.15 strain and T = 200 K and partial stress relief due to the formation of a liquid region at 0.15 and 264 K.

Considering the failure mechanisms of the mW model at 50 K, the response displays the same brittle cleavage seen for the TIP4P/Ice model. For the higher temperatures, however, the yield drop is achieved by a different mechanism. This is exemplified in particular by the behavior at $T = 200$ K. Instead of a complete stress relief, there is only a partial drop at the yield point, followed by a renewed stress build-up upon further straining. Inspection of the atomic configurations around the yield drop reveals that the incomplete stress relief is achieved by a plastic deformation event involving the nucleation of a dislocation dipole. This is visualized in Fig. 3, where the two thick lines represent the dislocation cores as obtained using the Dislocation Extraction Algorithm (DXA) algorithm[74] in OVITO and the red arrows describe their respective opposite Burgers vectors. They are of the $\frac{1}{6}[0\bar{2}23]$ type, which form imperfect dislocations combining the Burgers vectors of an in-basal-plane Shockley partial and an out-of-basal-plane imperfect dislocation with Burgers vectors of $\frac{1}{3}[0\bar{1}10]$ and $\frac{1}{2}[0001]$ types, respectively.[75,76] The dislocations are predominantly of edge character, and at the stage shown in the picture, the formation of the dipole is almost complete, with both dislocations still touching each other in the center. Since the in-basal-plane component of the opposing Burgers vectors corresponds precisely to that of a Shockley partial, both dislocations bound a stacking-fault area shown by the atoms in blue. Upon further straining, the two dislocations of the dipole fully detach, resulting in two almost straight dislocations along the $[0\bar{1}10]$ directions enclosing a rectangular area of stacking fault. Finally, at the highest temperature of 269 K, which is ~5 K below the melting temperature for the mW model, the yield drop is accompanied by complete melting.

To assess possible anisotropies in the response, we repeat the same deformation simulations but now applying tensile strain along the $[0\bar{1}10]$-axis. The resulting stress-strain response for the 12 800-molecule cell and both water models is displayed in the second row of Fig. 1. For the TIP4P/Ice model, the response curves are qualitatively similar to their c-axis counterparts for all temperatures, displaying a regular elastic rise followed by a single yield drop. In quantitative terms, compared to deformation along the c-axis, the yield stress for the TIP4P/Ice model is ~0.1-0.2 GPa lower. At $T = 50$ K, the yield drop is caused by complete cleavage, while at the higher temperatures, stress relief is achieved by the appearance of disordered/melted areas across the system and rotations of the remaining crystalline regions.

The mW model, on the other hand, behaves very differently. At 50 K, for instance, for which the c-axis response displays the usual rise followed by a single yield drop, as shown in Fig. 2, the tensile stress develops a non-monotonic response. It is characterized by a sequence of two rises separated by partial drops. Inspection of atomistic configurations along these sequences reveals that, instead of a yield drop, the system first passes through a structural phase transition before the onset of plastic deformation. This is shown in Fig. 4, which depicts atomic snapshots along the straining process. Between strains of ~0.20 and ~0.25, the system undergoes a phase transition to a different crystalline phase, followed by a stress drop close to ~0.30, where the cell has returned to a deformed Wurtzite structure accompanied by amorphous regions. The other crystalline phase that appears during the straining process retains a hexagonal structure, as is evident from the snapshot at the strain value of 0.25 in Fig. 4. In fact, this crystalline phase has the structure of a strained layered honeycomb lattice in which the armchair-like puckered hexagonal rings[1] of the ice I_h lattice have become planar, lying perpendicular to the c-axis. The stacking of the graphene-like layers is such that the hexagons of subsequent layers are shifted relative to each other along the $[2\bar{1}\bar{1}0]$ direction by ~0.27 Å, as shown in Fig. 5. The structure maintains the four-fold coordination of oxygen atoms, but the angles between pairs of bonds are severely distorted compared to a tetrahedral arrangement. In particular, the angle between the out-of-plane bond and the in-plane bond varies between 88° and 90°. For the same reason, the layered honeycomb structure also does not seem to be related to the cubic ice I_c phase previously observed in the mW model.[56] Like ice I_h, cubic ice features puckered hexagonal rings, with the only difference being their boat-like arrangement compared to the armchair conformation in ice I_h.

To the best of our knowledge, this phase has not been observed in water and it is likely to be an artifact of the mW model.

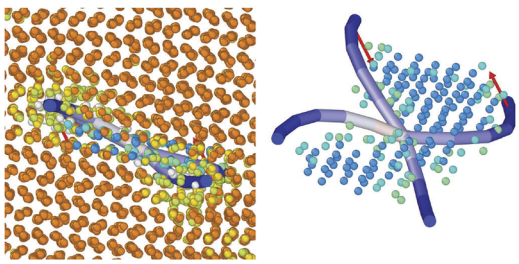

FIG. 3. Atomistic configurations during tensile deformation along the [0001] axis for the mW model and the 12 800-molecule cell at 200 K and a strain of 0.193. Thick lines depict dislocation lines of opposite Burgers vectors shown as red arrows. The left panel shows the view along the $[0\bar{1}10]$ direction. The right panel only displays the oxygen atoms in the stacking fault area (blue spheres) and the dislocations that delimit its bounds. Both dislocations still touch near the center of the image. Coloring of dislocation indicates its character, with blue and red representing edge and screw character, respectively.

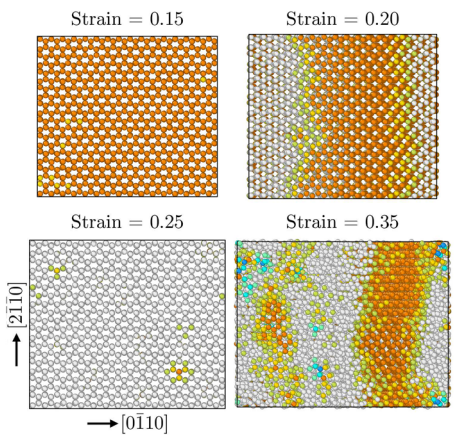

FIG. 4. Typical atomistic configurations during tensile deformation along the $[0\bar{1}10]$ axis for the mW model and the 12 800-molecule cell at 50 K. Crystalline phase reached at a strain of 0.25 corresponds to layered honeycomb structure.

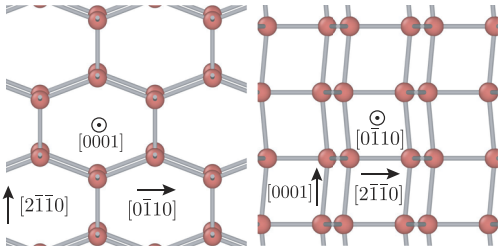

FIG. 5. Crystal structure of layered honeycomb phase strained along the [0$\bar{1}$10] direction. Bonds connect nearest neighbors. The left panel shows view along the *c*-axis. Two shown graphene-like sheets are subsequent layers along the *c*-axis. Their relative in-plane displacement is ~0.27 Å in the [2$\bar{1}\bar{1}$0] direction. The right panel depicts view along the [0$\bar{1}$10] direction. Relative shifts of subsequent layers give rise to the zig-zag-like structure along the *c*-axis.

For 200 K and 269 K, the phase transition does not take place and the yield drops in the stress-strain curves are associated with the dislocation activity. For instance, the first yield drop at 269 K is associated with the nucleation of a dipole of perfect edge dislocations with Burgers vectors of the type $\frac{1}{3}[\bar{2}110]$ and their line directions along the [0001] axis, as pictured in Fig. 6 (multimedia view). The subsequent saw-tooth-like evolution of the stress-strain curve upon further straining involves a number of dislocation-related events, including dipole annihilation and re-nucleation.

B. Compressive deformation

Next, we explore the response of the systems under compressive uniaxial deformation. The top row of Fig. 7 presents the stress-strain response for compressive deformation along the [0001]-axis on the 12 800-molecule cell, comparing the two water models at the same temperatures and strain rate as those considered for the tensile deformations. Again, for small strains, all systems display linear elastic behavior with Young's moduli consistent with the values reported in Sec. III A. Notably, for the TIP4P/Ice model at 50 K, the elastic response suddenly changes slope as the compressive strain exceeds 0.13. Inspection of the atomic structure shows that this sudden change of the slope in the stress-strain curve can be attributed to a distortion in the alignment of the O–O nearest-neighbor network as exemplified in Fig. 8. This

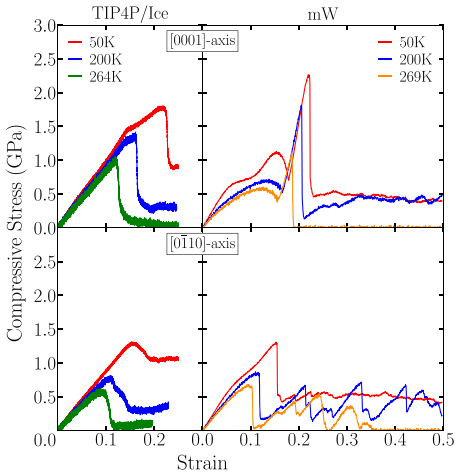

FIG. 7. Stress-strain curves for the compressive deformation at strain rate of 5×10^7 s^{-1} along the c-axis and the [0$\bar{1}$10] axis for TIP4P/Ice and mW models for the 12 800-molecule cell at different temperatures.

distorted structure continues to respond elastically until reaching the yield point close to a strain of ~0.22, after which the stress is partially relieved in a manner similar to that seen in the tensile deformations, with the appearance of large-scale disordering as well as substantial deformation and rotations of the remaining crystalline regions. At 200 K and 264 K, the yield points occur at smaller deformations and the low-temperature distorted structure no longer appears. The stress-relief mechanisms, on the other hand, are basically the same although at 264 K, the disordered regions are manifestly liquid in nature, displaying substantial diffusion.

For the mW model, although the elastic moduli at the initial stages of deformation are quantitatively similar to those of the tensile deformation test, the compressive elastic response is much more non-linear in the strain interval between ~0.05 and ~0.18. Surprisingly, further increasing the deformation gives rise to a second, mostly linear, elastic regime regardless of temperature. Inspection of the atomistic structure reveals that the sudden change into a steep second linear elastic regime is due to the same phase transition to the layered honeycomb structure shown in Fig. 5, in which the buckled hexagons in the Wurtzite structure become planar, here under the influence of the compressive stress along the *c*-axis. Finally, at

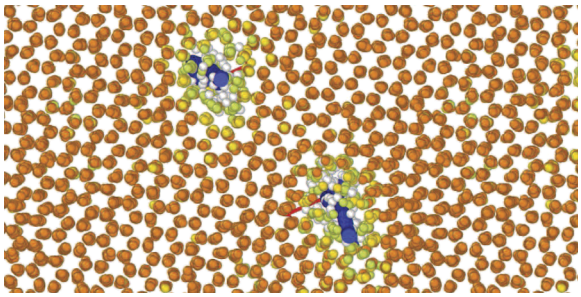

FIG. 6. Atomistic configuration viewed along the [0001] axis during tensile deformation along the [0$\bar{1}$10] axis (vertical direction in the figure) for the mW model at 269 K and a strain of 0.138. Thick blue lines depict dislocations of opposite Burgers vectors shown as red arrows. To better visualize the interactions between the dislocations, the view in the multimedia file displays the simulation cell periodically repeated 3 and 2 times, respectively, in the horizontal and vertical directions. Multimedia view: https://doi.org/10.1063/1.5048517.1

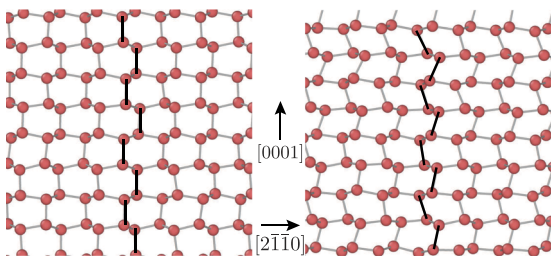

FIG. 8. Excerpt of the crystal structure of TIP4P/Ice model at 50 K compressed along the [0001] direction. Hydrogen atoms are not shown for clarity. Gray lines connect nearest-neighbor oxygen pairs. The left and right panel shows views below and above 0.13 strain, respectively. The oxygen-oxygen nearest-neighbor pairs that are aligned along the *c* axis below 0.13 strain develop into a zig-zag pattern, as highlighted by the thick black lines.

a strain in the range between 0.2 and 0.22, a marked single yield drop occurs. While at 269 K, the drop involves complete melting, and for the lower two temperatures, the stress relief is achieved by substantial disordering combined with appreciable deformation and rotations of the remaining crystalline regions.

The bottom row of Fig. 7 depicts the stress-strain responses for compressive uniaxial deformation along the $[0\bar{1}10]$ direction. As for the tensile deformation case, the anisotropy of the response for the TIP4P/Ice model is only modest. While the values of the yield stresses for compression along the $[0\bar{1}10]$ axis are somewhat lower in comparison to those for the [0001] direction, the failure mechanisms are the same. For the mW model, on the other hand, the response is again strongly anisotropic, with stress-strain curves that are qualitatively very distinct for both compression directions. For 200 K and 269 K, they display similar saw-tooth-like behavior as that observed for the tensile deformations. The origin of the serrated curves is again due to the dislocation activity, as visualized in Fig. 9. The two thick lines again represent the dislocation cores as obtained using the DXA algorithm[74] in OVITO, and the red arrows describe their respective opposite Burgers vectors. They are of the $\frac{1}{3}[1\bar{2}10]$ type, which form perfect dislocations,[76] and they are predominantly of edge character.

C. Influence of cell size and strain rate

To assess the extent to which the size of the used computational cell affects the obtained results, we repeat the tensile and compressive simulations using the larger cell containing 93 312 molecules at the same strain rate of $\dot{\varepsilon} = 5 \times 10^7$ s^{-1}. We find that the cell size does not fundamentally alter the results for both models, neither under tensile nor compressive deformation. This is illustrated in Fig. 10 which compares the compressive stress-strain curves for both cell sizes, with the results for the large cell depicted using dashed lines. The values of the yield stresses and strains for the two models are essentially unaffected, and the failure modes are also the same. In particular, for the mW model, the deformation simulations display the same serrated character associated with the dislocation activity and feature the same phase transition from the Wurtzite to the layered honeycomb structure.

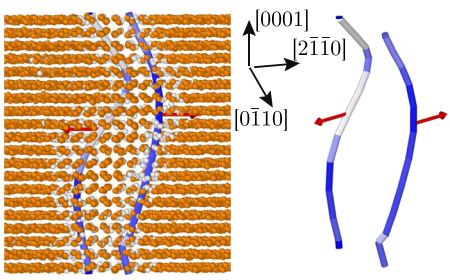

FIG. 9. Atomistic configurations during compressive deformation along the $[0\bar{1}10]$ axis for the mW model and the 12 800-molecule cell at 200 K and a strain of 0.25. Thick lines depict a dislocation dipole, of opposite Burgers vectors shown as red arrows, that are immersed in the atomistic structure. The left panel shows view along the $[0\bar{1}10]$ direction. The right panel only displays a perspective view of the dislocation dipole, and Burgers vectors correspond to the $\frac{1}{3}[1\bar{2}10]$ direction. Coloring of dislocation indicates its character, with blue and red representing edge and screw character, respectively.

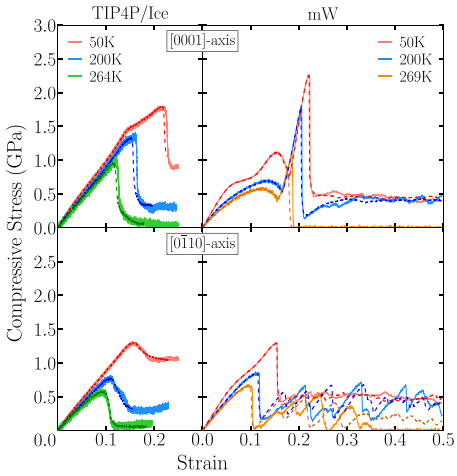

FIG. 10. Sample size influence on the stress-strain curves for compressive deformation at a strain rate of 5×10^7 s^{-1} and a variety of temperatures. Full and dashed lines represent data for 12 800 and 93 312-molecule cells, respectively.

We also investigated the effect of the applied strain rate on the obtained results. First we carried out a number of deformation simulations at a strain rate of 5×10^8 s^{-1}, an order of magnitude larger than that used to obtain the results described in Secs. III A and III B. This increase does not give rise to fundamentally different mechanisms of stress relief for neither of the models. For the mW model, we were also able to execute deformation simulations at a strain rate an order of magnitude lower, at 5×10^6 s^{-1}. Again, the mW model displays the same behavior, showing both brittle cleavages in tension for the lowest temperatures as well as the dislocation activity for higher temperatures. Due to the elevated computational cost associated with the long-range electrostatics, it has not been possible to carry out deformation simulations for the TIP4P/Ice model at a strain rate lower than 5×10^7 s^{-1}.

D. Discussion

The results presented in Secs. III A–III C clearly demonstrate the fundamentally different mechanical responses of both water models. For the all-atom TIP4P/ice model, with the exception for low-temperature tensile brittle cleavage, the main mechanism for uniaxial stress relief is large-scale amorphization or melting. The coarse-grained mW model, on the other hand, in addition to also failing by brittle cleavage at low temperatures, uniaxial failure occurs mainly by the usual plastic deformation mechanism involving nucleation and motion of lattice dislocations. In this sense, the mW model may be regarded as more ductile compared to TIP4P/Ice.

Indeed, the fact that mW behaves in such a malleable manner, even at strain rates that are substantially higher than those applied in typical experiments, indicates that the mW description of ice I_h is much too ductile. Uniaxial deformations carried out in the laboratory[77] have shown that single-crystal ice I_h deforms in a brittle manner already at strain rates $\sim 10^{-2}$ s^{-1}, which is 4-5 orders of magnitude slower than the deformation rates used in our simulations.

An interesting issue concerns the origin of the very different behaviors of TIP4P/Ice and mW. In addition to the very distinct functional forms describing cohesion, a key difference between them is the absence of explicit protons in the mW model. This means that the description of the hydrogen bond (HB) in the mW model does not capture its fundamental asymmetry, with one molecule donating a proton while the other acts as acceptor. While disregarding the HB asymmetry does not seem to prevent the model from correctly reproducing several thermodynamic properties of water and ice,[38] it may preclude it from capturing the essence of kinetic processes that involve the breaking and reformation of HBs.

A particular example of such a process in ice I_h involves the formation and motion of dislocations. A key element of the ice I_h structure is its proton-disordered character and, as analyzed in detail by Glen,[1,78] this randomness acts as an obstacle to both the formation as well as the movement of dislocations. This is so because when two molecular planes are initially bonded by randomly oriented HBs, shearing one plane with respect to the other will inevitably lead to mismatching hydrogen-bond conditions, for instance, having two proton donor or acceptor molecules instead of having a pair with one of each. This implies that after breaking a HB under shear, its reformation may not be topologically possible without additional molecular rotations, hampering the shearing process. The fact that the proton disorder is absent within the mW description is therefore a substantial facilitating ingredient in both the nucleation and motion of dislocations, inadvertently enhancing the model's malleability.

IV. SUMMARY

In summary, we have used molecular dynamics simulations to investigate the uniaxial-deformation response of ice I_h as described by the all-atom TIP4P/Ice potential and the coarse-grained mW model. Considering tensile and compressive uniaxial deformations along the [0001] and [$0\bar{1}10$] crystallographic directions for a series of different temperatures, we classify the respective failure mechanisms and assess their sensitivity to strain rate and cell size. The TIP4P/Ice model fails by either brittle cleavage under tension at low temperatures or large-scale amorphization/melting at higher temperatures. The mW potential, on the other hand, behaves in a much more ductile manner, displaying numerous cases in which stress relief is achieved by the nucleation and subsequent activity of lattice dislocations. In fact, given that mW behaves in such a malleable manner even at strain rates that are substantially higher than those applied in typical experiments indicates that the mW description of ice I_h is overly ductile. A possible factor in this enhanced malleability is the absence of explicit protons in the mW model, disregarding the fundamental asymmetry of the hydrogen bond that plays an important role in the nucleation and motion of lattice dislocations in ice I_h.

ACKNOWLEDGMENTS

We acknowledge support from Capes, CNPq, and Fapesp Grant Nos. 2013/08293-7 and 2016/23891-6. The authors acknowledge the National Laboratory for Scientific Computing (LNCC/MCTI, Brazil) for providing HPC resources of the SDumont supercomputer, URL: http://sdumont.lncc.br. Part of the simulations was carried out at CCJDR-IFGW-UNICAMP, CENAPAD-SP (Brazil) and TOKO-FCEN-UNCuyo (Argentina).

[1] V. F. Petrenko and R. W. Whitworth, *Physics of Ice* (Oxford University Press, New York, 1999).
[2] E. M. Schulson, JOM **51**, 21 (1999).
[3] E. Schulson and P. Duval, *Creep and Fracture of Ice* (Cambridge University Press, 2009).
[4] E. Reusch, Ann. Phys. **197**, 573 (1864).
[5] J. Glen and M. Perutz, J. Glaciol. **2**, 397 (1954).
[6] J. Currier and E. Schulson, Acta Metall. **30**, 1511 (1982).
[7] M. A. Lange and T. J. Ahrens, J. Geophys. Res. **88**, 1197, https://doi.org/10.1029/jb088ib02p01197 (1983).
[8] R. Andrews, J. Glaciol. **31**, 171 (1985).
[9] S. J. Jones, J. Phys. Chem. B **101**, 6099 (1997).
[10] J. Dempsey, R. Adamson, and S. Mulmule, Int. J. Fract. **95**, 347 (1999).
[11] E. M. Schulson, Eng. Fract. Mech. **68**, 1839 (2001).
[12] S. J. Jones, R. E. Gagnon, A. Derradji, and A. Bugden, Can. J. Phys. **81**, 191 (2003).
[13] P. K. Dutta, D. M. Cole, E. M. Schulson, D. S. Sodhi *et al.*, Int. J. Offshore Polar Eng. **14**, 182 (2004).
[14] H. Kim and J. N. Keune, J. Mater. Sci. **42**, 2802 (2007).
[15] M. Shazly, V. Prakash, and B. A. Lerch, Int. J. Solids Struct. **46**, 1499 (2009).
[16] A. Combescure, Y. Chuzel-Marmot, and J. Fabis, Int. J. Solids Struct. **48**, 2779 (2011).
[17] T. Sain and R. Narasimhan, Int. J. Solids Struct. **48**, 817 (2011).
[18] X. Wu and V. Prakash, Cold Reg. Sci. Technol. **118**, 1 (2015).
[19] J. Pernas-Sánchez, D. A. Pedroche, D. Varas, J. López-Puente, and R. Zaera, Int. J. Solids Struct. **49**, 1919 (2012).
[20] J. Pernas-Sánchez, J. A. Artero-Guerrero, D. Varas, and J. López-Puente, Exp. Mech. **55**, 1669 (2015).
[21] C. Qi, J. Lian, Q. Ouyang, and X. Zhao, Lat. Am. J. Solids Struct. **14**, 1669 (2017).
[22] D. L. Silva Junior and M. de Koning, Phys. Rev. B **85**, 024119 (2012).
[23] S. Ahmad, M. Ohtomo, and R. W. Whitworth, Nature **319**, 659 (1986).
[24] S. Ahmad and R. W. Whitworth, Philos. Mag. A **57**, 749 (1988).
[25] C. Shearwood and R. W. Whitworth, Philos. Mag. A **64**, 289 (1991).
[26] C. Shearwood and R. Whitworth, Acta Metall. Mater. **41**, 205 (1993).
[27] J. Kacher and I. M. Robertson, Philos. Mag. **96**, 1437 (2016).
[28] L. A. Zepeda-Ruiz, A. Stukowski, T. Oppelstrup, and V. V. Bulatov, Nature **550**, 492 (2017).
[29] M. S. Duesbery and G. Y. Richardson, Crit. Rev. Solid State Mater. Sci. **17**, 1 (1991).
[30] V. V. Bulatov, J. F. Justo, W. Cai, S. Yip, A. S. Argon, T. Lenosky, M. de Koning, and T. Diaz de la Rubia, Philos. Mag. A **81**, 1257 (2001).
[31] O. Mishima and H. E. Stanley, Nature **396**, 329 (1998).
[32] J. L. F. Abascal, E. Sanz, R. García Fernández, and C. Vega, J. Chem. Phys. **122**, 234511 (2005).
[33] C. Vega, J. L. F. Abascal, E. Sanz, L. G. MacDowell, and C. McBride, J. Phys.: Condens. Matter **17**, S3283 (2005).
[34] R. García Fernández, J. L. F. Abascal, and C. Vega, J. Chem. Phys. **124**, 144506 (2006).
[35] C. Vega, E. Sanz, J. L. F. Abascal, and E. G. Noya, J. Phys.: Condens. Matter **20**, 153101 (2008).
[36] R. Handel, R. L. Davidchack, J. Anwar, and A. Brukhno, Phys. Rev. Lett. **100**, 036104 (2008).
[37] Y. Liu, A. Z. Panagiotopoulos, and P. G. Debenedetti, J. Chem. Phys. **131**, 104508 (2009).
[38] V. Molinero and E. B. Moore, J. Phys. Chem. B **113**, 4008 (2009).
[39] L. G. MacDowell and C. Vega, J. Phys. Chem. B **114**, 6089 (2010).
[40] N. Kastelowitz, J. C. Johnston, and V. Molinero, J. Chem. Phys. **132**, 124511 (2010).
[41] J. L. Aragones, L. G. MacDowell, and C. Vega, J. Phys. Chem. A **115**, 5745 (2011).
[42] D. T. Limmer and D. Chandler, J. Chem. Phys. **135**, 134503 (2011).
[43] E. B. Moore and V. Molinero, Nature **479**, 506 (2011).
[44] E. B. Moore and V. Molinero, Phys. Chem. Chem. Phys. **13**, 20008 (2011).
[45] J. C. Johnston and V. Molinero, J. Am. Chem. Soc. **134**, 6650 (2012).

[46]Y. Liu, J. C. Palmer, A. Z. Panagiotopoulos, and P. G. Debenedetti, J. Chem. Phys. **137**, 214505 (2012).
[47]T. D. Shepherd, M. A. Koc, and V. Molinero, J. Phys. Chem. C **116**, 12172 (2012).
[48]D. T. Limmer and D. Chandler, J. Chem. Phys. **138**, 214504 (2013).
[49]E. Sanz, C. Vega, J. R. Espinosa, R. Caballero-Bernal, J. L. F. Abascal, and C. Valeriani, J. Am. Chem. Soc. **135**, 15008 (2013).
[50]A. H. Nguyen and V. Molinero, J. Phys. Chem. B **119**, 9369 (2015).
[51]A. Zaragoza, M. M. Conde, J. R. Espinosa, C. Valeriani, C. Vega, and E. Sanz, J. Chem. Phys. **143**, 134504 (2015).
[52]G. A. Cisneros, K. T. Wikfeldt, L. Ojamäe, J. Lu, Y. Xu, H. Torabifard, A. P. Bartók, G. Csányi, V. Molinero, and F. Paesani, Chem. Rev. **116**, 7501 (2016).
[53]J. R. Espinosa, A. Zaragoza, P. Rosales-Pelaez, C. Navarro, C. Valeriani, C. Vega, and E. Sanz, Phys. Rev. Lett. **117**, 135702 (2016).
[54]J. R. Espinosa, C. Navarro, E. Sanz, C. Valeriani, and C. Vega, J. Chem. Phys. **145**, 211922 (2016).
[55]J. R. Espinosa, C. Vega, and E. Sanz, J. Phys. Chem. C **120**, 8068 (2016).
[56]L. Lupi, A. Hudait, B. Peters, M. Grünwald, R. Gotchy Mullen, A. H. Nguyen, and V. Molinero, Nature **551**, 218 (2017).
[57]J. Gelman Constantin, M. A. Carignano, H. R. Corti, and I. Szleifer, J. Phys. Chem. C **119**, 27118 (2015).
[58]J. Wu, F. Ning, T. T. Trinh, S. Kjelstrup, T. J. H. Vlugt, J. He, B. H. Skallerud, and Z. Zhang, Nat. Commun. **6**, 8743 (2015).
[59]S. H. Min and M. L. Berkowitz, J. Chem. Phys. **148**, 144504 (2018).
[60]W. L. Jorgensen and J. D. Madura, Mol. Phys. **56**, 1381 (1985).
[61]F. H. Stillinger and T. A. Weber, Phys. Rev. B **31**, 5262 (1985).
[62]J. A. Hayward and J. R. Reimers, J. Chem. Phys. **106**, 1518 (1997).
[63]A. Rahman and F. H. Stillinger, J. Chem. Phys. **57**, 4009 (1972).
[64]S. Plimpton, J. Comput. Phys. **117**, 1 (1995).
[65]M. Parrinello and A. Rahman, J. Appl. Phys. **52**, 7182 (1981).
[66]G. J. Martyna, D. J. Tobias, and M. L. Klein, J. Chem. Phys. **101**, 4177 (1994).
[67]W. Shinoda, M. Shiga, and M. Mikami, Phys. Rev. B **69**, 134103 (2004).
[68]T. Schneider and E. Stoll, Phys. Rev. B **17**, 1302 (1978).
[69]J.-P. Ryckaert, G. Ciccotti, and H. J. Berendsen, J. Comput. Phys. **23**, 327 (1977).
[70]R. W. Hockney, *Computer Simulation Using Particles* (Taylor & Francis Group, 2017).
[71]P. H. Gammon, H. Kiefte, and M. J. Clouter, J. Phys. Chem. **87**, 4025 (1983).
[72]E. Maras, O. Trushin, A. Stukowski, T. Ala-Nissila, and H. Jönsson, Comput. Phys. Commun. **205**, 13 (2016).
[73]A. Stukowski, Modell. Simul. Mater. Sci. Eng. **18**, 015012 (2010).
[74]A. Stukowski, V. V. Bulatov, and A. Arsenlis, Modell. Simul. Mater. Sci. Eng. **20**, 085007 (2012).
[75]A. Berghezan, A. Fourdeux, and S. Amelinckx, Acta Metall. **9**, 464 (1961).
[76]D. Hull and D. Bacon, *Introduction to Dislocations* (Butterworth-Heinemann, 2001).
[77]M. A. Rist, J. Phys. Chem. B **101**, 6263 (1997).
[78]J. Glen, Phys. Kondens. Mater. **7**, 43 (1968).